UV-Selective Optically Transparent Zn(O,S)-Based Solar Cells

Alex J. Lopez-Garcia,* Andreas Bauer, Robert Fonoll Rubio, David Payno, Zacharie Jehl Li-Kao, Samrana Kazim, Dimitrios Hariskos, Victor Izquierdo-Roca, Edgardo Saucedo, and Alejandro Pérez-Rodríguez

This work reports experimental evidence of a photovoltaic effect in transparent UV-selective Zn(O,S)-based heterojunctions. Zn(O,S) has a strong interest for the development of UV-selective solar cells with high transparency in the visible region, required for the development of nonintrusive building-integrated photovoltaic (BIPV) elements as transparent solar windows and glass-based solar façades. By anion alloying, Zn(O,S) mixed crystal absorbers can be fabricated with different sulfur content across the whole compositional range. This allows adjustment of the bandgap of the absorbers in the 2.7–2.9 eV region, maximizing absorption in the UV, while keeping a high level of transparency. Zn(O,S) alloys with composition corresponding to $S/(S+O)$ content ratios of 0.6 are successfully grown by sputtering deposition, and first glass/FTO/NiO/Zn(O,S)/ITO device prototypes are produced. The resulting devices present an average visible transmittance (AVT) of 75% and present photovoltaic effect. By introducing a thin C_{60} film as electron transport layer (ETL), charge extraction is enhanced, and devices show an efficiency of 0.5% and an AVT > 69%. The transparency of these devices can potentially allow for their ubiquitous installation in glazing systems as part of nonintrusive BIPV elements or to power Internet of Things (IoT) devices and sensors as an integrated transparent component.

Building-integrated photovoltaic (BIPV), which nowadays represents about 2% of the PV market, is an area that has the aim of easing local energy production by providing buildings with both conventional and novel ubiquitous and efficient PV devices, with the ideal goal of reaching net-zero energy consumption buildings (nZEB).[1] These applications result in an increased interest in obtaining fully transparent PV (TPV) devices in the visible range, while they can selectively absorb UV and/or IR wavelengths.[2] Such devices present a high potential for integration in glazing systems and smart windows as nonintrusive BIPV elements. Other novel applications include devices that could be integrated as functional active harvesting components to power optoelectronic devices such as sensors, electrochromic windows, or Internet of Things (IoT) devices.[3,4] An interesting strategy for the development of these devices is the combination of UV-selective wide bandgap inorganic solar cells and

A. J. Lopez-Garcia, R. Fonoll Rubio, Dr. Z. Jehl Li-Kao, Dr. V. Izquierdo-Roca, Prof. A. Pérez-Rodríguez
Solar Energy Materials and Systems
Institut de Recerca en Energia de Catalunya (IREC)
Jardins de les Dones de Negre, 1, 2ª pl, Sant Adrià del Besòs 08930, Barcelona, Spain
E-mail: alopez@irec.cat

Dr. A. Bauer, Dr. D. Hariskos
Photovoltaik Materialforschung
Zentrum für Sonnenenergie- und Wasserstoff-Forschung Baden-Württemberg
Meitnerstr. 1, Stuttgart 70563, Germany

The ORCID identification number(s) for the author(s) of this article can be found under https://doi.org/10.1002/solr.202000470.

D. Payno, Dr. S. Kazim
BCMaterials
Basque Center for Materials, Applications and Nanostructures
Bld. Martina Casiano, UPV/EHU Science Park, Barrio Sarriena s/n
Leioa 48940, Spain

Dr. S. Kazim
IKERBASQUE
Basque Foundation for Science
Bilbao 48013, Spain

Prof. E. Saucedo
Photovoltaic Group
Department Enginyeria Electrònica
Universitat Politècnica Catalunya
c/ Jordi Girona 3-1, Barcelona 08034, Spain

Prof. A. Pérez-Rodríguez
IN2UB
Departament d'Enginyeria Electrònica i Biomèdica
Universitat de Barcelona
Carrer de Martí i Franquès 1, Barcelona 08028, Spain

IR-selective organic solar cells in a hybrid tandem-like structure.[5] Maximizing UV absorption in the UV-selective top cells has an additional interest, as this allows preventing UV-induced degradation of the subjacent IR-selective organic device in the cell structure. Wavelength-selective TPV applications can thus expand the applications in the PV industry, especially within the BIPV sector.

Focusing on UV-selective TPV devices, oxide materials are very interesting for the development of these devices because they are stable, inexpensive, abundant, easy to process, and typically nontoxic. Among them, ZnO is an interesting material which has been intensively studied for many decades. It presents high absorption coefficient ($\alpha(\lambda) > 10^4 \, cm^{-1}$ for $\lambda < 390$ nm) and a direct energy bandgap of 3.37 eV.[6,7] To date, state-of-the art UV-selective solar cells are mainly based on the use of ZnO as the absorber material.[8–13]

However, there are some important caveats that limit the use of ZnO for such solar cells. First, related to polarity and charge transport properties, being the fact of lack of bipolarity (i.e., p-type ZnO) which prevents the fabrication of homojunctions in conventional p–n configuration and also the synthesis of p-ZnO as absorber.[6,7,14] ZnO, if undoped, presents mild n-type character and is highly resistive, presenting poor transport properties such as low carrier mobility. Absorbers with poor carrier transport, for example, a-Si, have thus resorted to alternative device configurations in which the absorber is sandwiched between two carrier-selective contacts, known as charge transport layers (CTLs).[15] This device architecture has also been widely used in perovskite systems, where the intrinsic absorber typically presents excellent transport properties.[16–18] It is thus relevant to study such architectures incorporating CTLs, which can be both organic or inorganic.

Second, and most important for UV-selective solar cells, the bandgap of ZnO (3.37 eV) is much higher than the UV spectral onset at around 2.7 eV. This implies that photons with energies below the bandgap energy of ZnO and down to the 2.7 eV onset will not be absorbed, resulting in a lower range of photon absorption in the UV spectral region and consequently in inherent efficiency losses. This is confirmed by the dependence of the efficiency on the absorber bandgap,[19] also simulated in this report using SCAPS.[20] The results of the simulation are presented in Figure S1, Supporting Information. As shown in this figure, using ZnO as absorber, the maximum efficiency (AM1.5G, $100 \, mW \, cm^{-2}$) of the device is limited at values below 0.3%, whereas decreasing the bandgap of the absorber down to 2.7 eV results in an increase in the efficiency limit to values slightly above 4%.

Hence, it is important to find a material that presents both high absorption in the UV and a bandgap closer to the UV spectral onset. None of the binary oxides fulfil this bandgap requirement. However, by anion alloying ZnO with sulfur (S), it is possible to fabricate Zn(O,S) mixed crystals. Zn(O,S) presents a bandgap energy bowing with a reported minimum value at 2.7 eV in the mid-compositional range.[21–24] By exploring intermediate sulfur/oxygen composition, the bandgap can be reduced to values closer to the visible region while still absorbing exclusively in the UV region, allowing the development of devices with colorless visible transparency. In this work, it is shown that it is indeed possible to fabricate Zn(O,S) layers with well-controlled $S/(S+O)$ relative content that can be used for the development of UV-selective transparent devices presenting a more optimal spectral match with the UV region and showing PV effect using different device configurations. Optical and electrical properties of the fabricated absorbers and devices are analyzed and discussed herein.

$ZnO_{1-x}S_x$ layers have been grown on glass/FTO and glass/FTO/NiO stacks with a target S relative content corresponding to $x = 0.6$ and a thickness of 105 nm. Layers on glass/FTO/NiO were subsequently used for the fabrication of planar heterojunction solar cells with structures Glass/FTO/NiO/Zn(O,S)/ITO and glass/FTO/NiO/Zn(O,S)/C_{60}/BCP/ITO (**Figure 1**). NiO was used as a hole-selective contact, C_{60} was used as an electron transport layer (ETL) in conjunction with a bathocuproine (BCP) nanometric layer acting as hole-blocking layer, and In_2O_3:SnO_2 (ITO) acted as the transparent front-contact of the solar cell. The fabrication process is described in detail in the Experimental Section. Optical and electrical characterization has been done on completed devices while Raman spectroscopy measurements were carried out on Glass/FTO/Zn(O,S) and glass/FTO/NiO/Zn(O,S)/C_{60} samples to assess the formation and the composition of the mixed crystal and to assess the correct deposition of the organic ETL, respectively.

Optical transmittance of the completed devices was measured by optical spectrophotometry (Figure 1c) within the UV–visible spectral range to assess the transparency of the absorber thin films and their absorption onset. From these measurements, it is possible to calculate the average visible transmittance (AVT) of the completed device, a paramount figure-of-merit in TPV, which gives information on the visible transparency coupled with the human eye's photopic response, thus providing weighted information on the transparency of the sample, including the perception of humans (see ref. [3] for a detailed description). It is also possible to give an estimation of the energy bandgap of the Zn(O,S) absorber via Tauc's plot, which was estimated at 2.83 eV (Figure S2, Supporting Information). This value is in good agreement with the bandgap estimated from the dependence of the bandgap of Zn(O,S) on the S relative content reported in refs. [22,23]. In Figure 1c, it can be observed that the devices are highly transparent in the visible range. The FTO substrate and back-contact, presented as reference, gives an idea on the upper limit of AVT that can be achieved (83%). The other two curves correspond to completed devices, with and without the C_{60} ETL layer for comparison. It can be observed that the devices present almost the same transmission curve. However, a slight drop in transmittance can be observed near the absorption onset region and in the visible range, as expected through the addition of the ultrathin ETL layer in the device architecture. The rest of the oxide films used present wide-bandgap above 3.5 eV, making them naturally transparent due to their energy bandgap. From these spectra, it was calculated that the AVT of the devices with and without the C_{60} ETL was 69.3% and 75.4%, respectively (**Table 1**). In Figure 1d, a picture of a device is shown as visual representation of the transparency of the device. The optical properties of the samples clearly show that they are suitable candidates for being used as an active transparent component in BIPV and other fields.

To check for the presence of the Zn(O,S) mixed crystal and confirm the composition of the Zn(O,S) absorbers, Raman spectroscopy measurements have been performed. The Raman
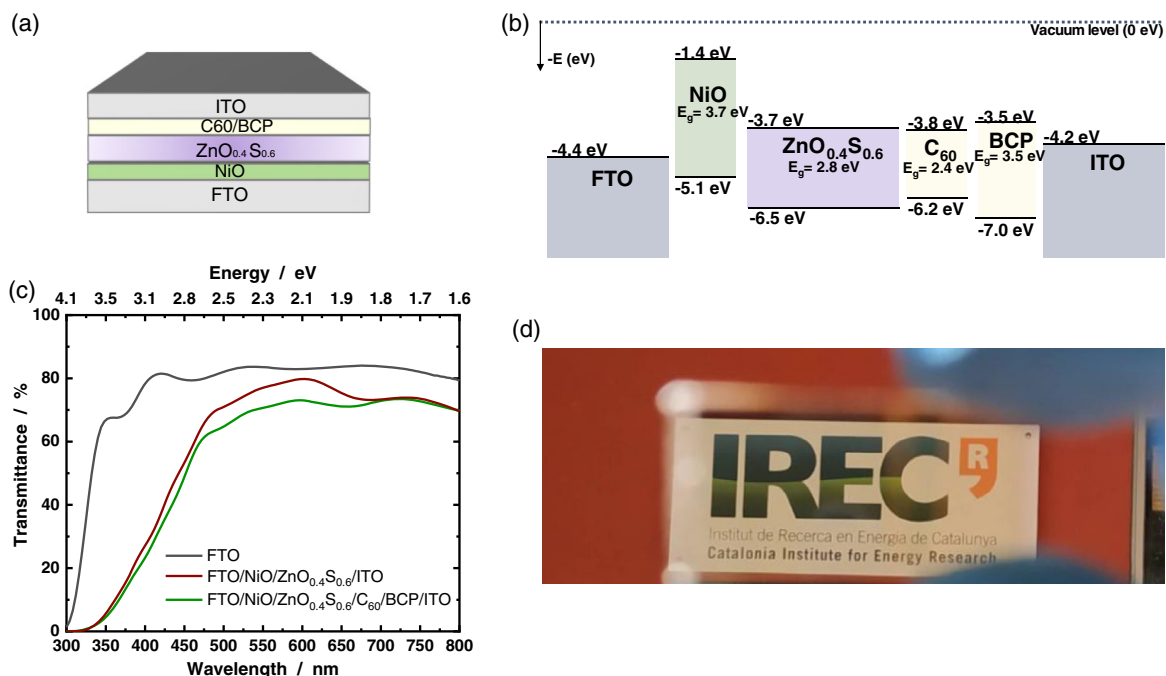
Figure 1. a) Schematic illustration of the fabricated TPV device architecture; b) Energy band diagram at equilibrium for the different layers in the system. c) Transmittance spectra of the devices FTO/NiO/Zn(O,S)/ITO and FTO/NiO/Zn(O,S)/C_{60}/BCP/ITO. FTO spectra is presented as reference and as upper limit indicator of device AVT. d) Picture taken at daylight in outdoor conditions. The picture presents a "see-through" image of the device, showing a white board with the IREC logo located at the building entrance.

Table 1. Summary of parameters and main results of fabricated TPV devices.

Device	AVT [%]	V_{oc} [V]	J_{sc} [mA cm^{-2}]	FF [%]	η [%]
FTO/NiO/ZnO$_{0.4}$S$_{0.6}$/ITO	75.4	0.265	0.11	32.6	<0.10
FTO/NiO/ZnO$_{0.4}$S$_{0.6}$/C$_{60}$/BCP/ITO	69.3	0.450	3.64	28.5	0.48

spectrum (**Figure 2**a) from $ZnO_{1-x}S_x$ system shows a two-mode behavior that is characteristic of the mixed crystal, with the presence of a ZnO-like peak (located at 574 cm^{-1} in ZnO) and a ZnS-like peak (located at 351 cm^{-1} in ZnS). The frequency of the ZnO peak shows a linear dependency with the $S/(S + O)$ composition ratio, whereas the frequency of the ZnS-like is not affected by the composition of the layers. Figure 2a shows
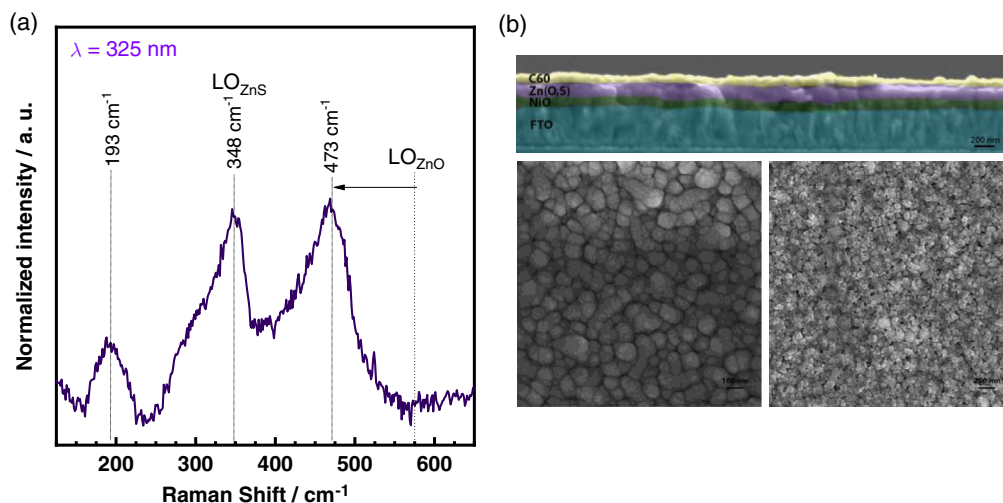

Figure 2. a) Raman spectrum of FTO/ZnO$_{1-x}$S$_x$ for relative sulfur content $x = S/(S + O) = 0.6$ acquired with 325 nm excitation wavelength. The main peaks observed are a characteristic Zn(O,S)-like mode at 193 cm^{-1}, the LO ZnS mode at 348 cm^{-1}, and the ZnO-like LO mode, shifted toward a lower Raman shift of 473 cm^{-1}. b) (top) CS-SEM pseudo-colored image of FTO/NiO/Zn(O,S)/C$_{60}$. (bottom-left) Top-view SEM image of Zn(O,S) layer. (bottom-right) Top-view SEM image of C$_{60}$ film.

the Raman spectra of the FTO/Zn(O,S) sample, obtained using monochromatic 325 nm excitation wavelength. The spectra show the main peaks characteristic of the $Zn(O_{1-x}S_x)$ mixed crystal. The ZnS-like peak is visible at about $348\,cm^{-1}$ (close to the frequency reported for the ZnS LO peak). The ZnO-like peak is observed at $473\,cm^{-1}$. This peak shift indicates an increase in the oxygen content with respect to the sulfur one in the Zn(O,S) structure.[22] The estimation of the $S/(S + O)$ content ratio in the layers has been performed considering the quantitative dependence of the position of the ZnO-like peak on the alloy composition reported in ref. [22], a methodology that allows to probe the formation of the alloy avoiding errors in composition due to segregation of ZnO/ZnS into secondary phases, confirming the value of $x = 0.6$ targeted for the layers experimentally grown. In addition, a band located at the $160–225\,cm^{-1}$ spectral region, with a peak at $193\,cm^{-1}$ is observed, attributed to fundamental overtones out of the Γ point of the Brillouin zone activated for the induced intrinsic disorder in the mixed crystal for the break of symmetry in the crystal structure due to S–O substitution.[22,25] In addition, to check for the correct deposition and crystallization of the fullerene layer, Raman measurements were carried out (Figure S3, Supporting Information) confirming the correct deposition of the film. Importantly, it should be noted that, as reported in refs. [23,26], even though this work relies on Zn(O,S) with relative sulfur content $x = 0.6$, there is a wide region of compositions that allow adjusting the bandgap of the absorbers between 2.7 and 2.9 eV. As shown in ref. [23], working in the composition range corresponding to values of x between $x = [0.3, 0.6]$ has a special interest, because in this range the bandgap as well as the conduction and valence bands of Zn(O,S) are similar for the different sulfur contents. Accordingly, in this range, the optoelectronic properties of the absorbers are not significantly affected by the variation in sulfur-relative content. This widens the choice of sulfur content to reduce the bandgap to the desired 2.7–2.9 eV range.

Field emission-scanning electron microscopy (FE-SEM) images were acquired to identify the different layers in the device and to assess the morphology of both the Zn(O,S) layer and the C_{60} layer (Figure 2b). The top image presents a cross-sectional pseudo-colored image of the device up to the fullerene layer. It can be observed that the layers are smooth and can be clearly identified, proving the correct deposition of the materials. The bottom-left image corresponds to a top-view image of the Zn(O,S) absorber layer. The Zn(O,S) layer is a compact film showing the formation of clusters of nano-sized grains. These clusters present grain sizes in the range of tens to hundreds of nanometers. The bottom-right image shows a top-view image of the C_{60} film. The film presents nanocrystalline size and some pores are present showing some degree of inhomogeneity in the processed film. Pore formation is detrimental for devices and should be avoided. To do this, two different approaches are envisaged, one involving a two-step process or bilayer, where a seed layer is formed and subsequently another layer is deposited to complete the desired thickness. Another approach would involve surface modification of Zn(O,S). Chemical or mechanical planarization of this surface would potentially decrease voids as the surface roughness plays a critical role in the growth of very thin films.

To characterize the photovoltaic properties of the devices, current density–voltage (J–V) measurements under solar simulator AM1.5G illumination ($100\,mWcm^{-2}$) were carried out. **Figure 3**a shows the results obtained for the fabricated devices corresponding to the Glass/FTO/NiO/Zn(O,S)/ITO and Glass/FTO/NiO/Zn(O,S)/C_{60}/BCP/ITO device architectures. These results and the parameters obtained are summarized in Table 1. These measurements confirm the existence of a photovoltaic effect in the heterojunction devices that is mainly attributed to the selective absorption of UV photons in the Zn(O,S) optically transparent layers and that Zn(O,S)-based heterojunction solar cells can be fabricated. The device without the C_{60} ETL presents still quite low short-circuit current density, in the order of $0.11\,mA\,cm^{-2}$, and a moderate open-circuit voltage of 0.256 V. These values serve as proof-of-concept of the PV functionality of the Zn(O,S) absorbers. However, an overall low efficiency, below 0.1% is observed for the nonoptimized FTO/NiO/Zn(O,S)/ITO device architecture. Nonetheless, the AVT is notably high, slightly over 75%.

Upon introduction of a C_{60} ETL together with an ultrathin BCP hole-blocking layer, the device performance is significantly
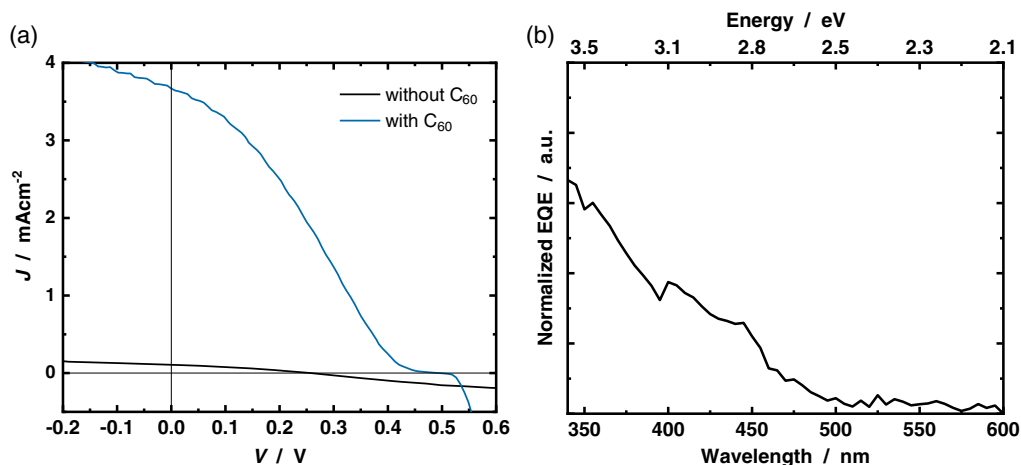
Figure 3. a) Photovoltaic characterization of fabricated TPV devices. J–V measurements under AM1.5G illumination for Zn(O,S) devices with S content $x = 0.6$, with (blue) and without (gray) the organic C_{60} ETL.

increased, due mainly to the increase in photocurrent and also (in a minor degree) to the increase in the photovoltage. The device presents a $J_{sc} = 3.64\,\text{mA cm}^{-2}$, a V_{oc} close to 0.5 V, and a low FF that yield an efficiency of 0.48% (Table 1). This device still shows an AVT of 69.3%. With these parameters, it is possible to calculate a figure-of-merit in TPV, the light utilization efficiency (LUE), which is the product of efficiency times the AVT of the device.[3] The calculated value for this device gives LUE = 0.34%. This is significantly higher than the best values achieved up to now with UV ZnO solar cells, according to the table found in supplementary data reported in ref. [3]. Albeit promising, the PCE value is still too low. However, the results are promising and can lead to the realization of real-life application devices. As reported by Traverse et al. in ref. [3], PCEs in the range 2–5% are sufficient to autonomously power smart windows and low-power displays. Future strategies for increasing the PCE rely on the identification and replacement of the CTLs, especially in the case of the NiO hole-transport layer (HTL), which could potentially be replaced by other materials such as MoS_2 or MoO_3. In addition, the Zn(O,S) film can be optimized, in terms of fine tuning carrier concentration and morphology.

Taking now a closer look into the J–V characteristics of the hybrid device, there are some particularities in the shape of the curve that need to be carefully addressed. The nonconventional shape already indicates that the device presents some limitations in performance. First, due to the low FF and second, and most important in the analysis, two regions are observed with a special behavior. For voltages closer to the V_{OC}, there is a region that shows a constant current near to zero, instead of a monotonous increase toward a negative current density. This nondesired behavior has already been reported in previous works in the organic PV community, and it is commonly known as the "S-kink". The possible working mechanisms have been related to interface morphology, oxygen doping, and the presence of charged interfaces forming extraction and injection barriers.[27] This shows the critical role of interfacial phenomena in these solar cells.

The speculative interpretation of the presence of the S-kink in the Zn(O,S) solar cells is likely related to the formation of an interfacial barrier at the CTL/electrode interface and/or at the HTL/Zn(O,S), as supported by previous reports.[28–30] It results in a V_{OC} and FF deficit, which limits device efficiency. It is suggested that by introducing an ultrathin dipolar molecule layer, such as LiF, at the interface might alleviate this issue, due to the formation of an electric dipole that generates a localized polarization field minimizing the barrier. This would lead to a reduced interface recombination. Interfacial optimization can thus potentially remove the S-kink behavior and increase device efficiency. Replacing NiO by other well-suited HTL could also result in increased performance.

Finally, another interesting aspect in the J–V characteristics happens in the region $V \in [-0.2, 0.05]\,\text{V}$. A linear dependence of the photocurrent as a function of voltage is observed in this region. This particular behavior has been reported in organic planar heterojunctions with $CuPc/C_{60}$ and explained in the work by Jeong et al.,[31] by experiment and simulation. It has been shown that the linear dependence of the photocurrent with bias originates from the C_{60} layer due to an effect known as bulk

ionization photoconductivity. The maximum bulk ionization yield photocurrent has been calculated, reaching values below $0.7\,\text{mA cm}^{-2}$ for a 40 nm thick layer and of $0.35\,\text{mA cm}^{-2}$ for a 35 nm layer. The implications are that C_{60} can indeed participate actively in the PV effect due to this bulk ionization effect, but this is an additional or secondary effect that couples and is observed in the J–V curve under illumination at small forward and reverse bias. The PV effect can then be mainly attributed to the UV absorption by Zn(O,S) and to the formation of a hybrid donor–acceptor (D/A) interface with the fullerene layer that is involved in charge separation and in electron transport and collection through the ITO electrode. This hypothesis is supported also by the observation of PV effect in the devices without the C_{60} ETL.

To further confirm that the device presents selective UV absorption, spectral response measurements were carried out. Figure 3b shows the measured normalized external quantum efficiency (EQE) of the device containing the C_{60} layer. It can be seen that the EQE curve rises from 2.7 eV toward higher energies, suggesting that absorption indeed takes place in the UV region and that it is mostly related to absorption in Zn(O,S). The poor shape of the EQE curve indicates also that hole-extraction is limited, as seen by the low steepness of the curve in the lower energy region.

In summary, the fabrication of UV-selective transparent solar cells based on Zn(O,S) in a fully transparent device in a planar configuration incorporating transparent electrical contacts has been presented for the first time. Zn(O,S) mixed crystal absorbers were successfully synthesized in the intermediate range with sulfur-relative content $x = 0.6$, thus enabling the precise choice of bandgap and optical absorption onset, in this case around 2.8 eV. This material is deemed as better suited for UV-selective absorption and filtering, as compared with the most commonly studied ZnO, because of the possibility to adjust the bandgap of the absorber to values closer to the UV onset by controlling the absorber composition, resulting in a better spectral match for such application. It is critical to identify optimal electron and hole selective transport layers better suited to the Zn(O,S) wide bandgap absorbers. It would also be interesting to investigate other compositional regions in the Zn(O,S) system, as different crystal structures can be obtained in either O-rich region or in S-rich region and the bandgap energy can still be placed below 3 eV. The experimental confirmation on the existence of a photovoltaic effect in the synthesized Zn(O,S)-based devices is very promising and confirms the interest in the development of Zn(O,S) mixed crystal as absorber layers for UV-selective TPV applications with very high optical transparency and its potential use as active photovoltaic component. Other potential applications such as UV-photodetectors, powering IoT devices, UV-light-emitting diodes (LEDs), and tandem PV devices are also envisaged.

Experimental Section

Sample Preparation: The solar cells fabricated in this work present the structure Glass/FTO/NiO(40 nm)/ZnO$_{0.4}$S$_{0.6}$(105 nm)/ITO(190 nm) and Glass/FTO/NiO(40 nm)/ZnO$_{0.4}$S$_{0.6}$(105 nm)/C$_{60}$(35 nm)/BCP(5 nm)/ITO(190 nm). Commercial Glass/FTO substrates (Merck; $R_{sh} = 12\,\Omega\,\text{sq}^{-1}$) were used as substrate and back-contact for the solar cell devices. Prior to

deposition, substrates were first rinsed in distilled water, dried in Ar flux and afterward cleaned by subsequent baths in isopropanol and milli-Q H_2O in an ultrasonic bath at room temperature for 10 min each and then were dried with Ar flux. NiO films were deposited on FTO by electron beam evaporation (Oerlikon Univex 250). NiO pieces (Alfa Aesar; 3–12 mm, 99.995%) were used as evaporant in a 4cc Al_2O_3 liner (Neyco). The chamber was evacuated at a base pressure of 10^{-6} mbar before evaporation and the deposition took place at room temperature, with no intentional heating, at 10 kV and with an electron current of 9 mA, at a rate of 0.5 Å s^{-1} measured with a quartz crystal microbalance (Inficon SQC-310; Au 6 MHz sensor). Zn(O,S) layers were deposited by sputtering (von Ardenne CS730S) from mixed ZnO/ZnS targets. Deposition parameters were RF power density 0.95 W cm^{-2} (i.e., 300 W, growth rate $\approx$15–24 nm min^{-1}), total gas flow 20 sccm argon at 10 μbar. Prior deposition, all samples were heated to 150 °C (nominal) in vacuum and remained throughout on the heater while deposition. C_{60} solution was prepared by dissolving C_{60} (TCI, 99.5%) in 1,2-dichlorobenzene with a concentration of 10 mg mL^{-1}. The solution was filtered with a polytetrafluoroethylene (PTFE) filter of 0.42 μm pore size prior its use. Thin films were deposited by static spin-coating at 1500 rpm for 60 s and transferred to a preheated hotplate at 80 ºC in air for 2 min. BCP (TCI, 99.0%) was dissolved in dry IP at 0.6 mg mL^{-1}. BCP solution was filtered with a 0.22 μm pore-size filter and spin-coated at 5000 rpm for 30 s. To complete the device, a 190 nm thick ITO film was deposited by DC-Pulsed Magnetron Sputtering (Alliance CT-100). Prior to deposition, the chamber was evacuated at 10^{-7} mbar and the substrate was heated up to 200 °C. The ITO target (Neyco; In_2O_3/SnO_2 90/10 wt%, 4N) was presputtered to remove any surface contaminants with the shutter in closed configuration. The deposition took place at 200 °C at a working pressure of 3×10^{-3} mbar in a mixed Ar/O_2 atmosphere at 30/0.5 sccm, applying a DC power density of 1.9 W cm^{-2} to the target.

Characterization: UV–vis measurements were acquired with a dual-beam spectrophotometer setup (Perkin Elmer Lambda L35) in transmittance mode (light source and detector normal to sample's surface (i.e., 0°)) scanning from 300 to 800 nm.

Raman spectroscopy was performed with a FHR640 Horiba Jobin–Yvon spectrometer coupled to a Raman probe developed at Institut de Recerca en Energia de Catalunya (IREC) and a cryogenically cooled charge coupled device detector. Measurements were carried out in backscattering configuration and with a 325 nm UV laser as the excitation wavelength. An excitation power density of about 25 W cm^{-2} was used to inhibit thermal effects on the samples. The Raman shift was calibrated using a Si monocrystal reference and adjusting the Raman shift for the main Si band at 520 cm^{-1}.

FE-SEM images were acquired with a ZEISS Auriga Series system. The images were acquired at 5 kV, aperture of 20 μm, and working distance of around 4 mm with the InLens detector.

J–V measurements under illumination were carried out using a homemade setup consisting on a 150 W xenon broadband arc Lamp (Thorlabs SLS401) calibrated using a NREL-certified Si reference solar cell (Abet Technologies, Model 15150). Electrical measurements were carried out with a source-measure unit (Keithley 2400) in four-wire sense mode, controlled by the software Tracer (ReRa solutions) using a IEEE 488 GPIB Instrument Control Device (National Instruments GPIB-USB-HS).

EQE curves were obtained using a spectral response system (Bentham PVE300) calibrated with a Si photodiode.

Supporting Information

Supporting Information is available from the Wiley Online Library or from the author.

Acknowledgements

Conflict of Interest

The authors declare no conflict of interest.

Keywords

[1] G. Masson, I. Kaizuka, https://iea-pvps.org/wp-content/uploads/2020/02/5319-iea-pvps-report-2019-08-lr.pdf (accessed: March 2020).

[2] R. R. Lunt, *Appl. Phys. Lett.* **2012**, *101*, 043902.

[3] C. J. Traverse, R. Pandey, M. C. Barr, R. R. Lunt, *Nat. Energy* **2017**, *2*, 849.

[4] X. Lin, Y.-L. Loo, M. Sezen-Edmonds, N. C. Davy, J. Gao, A. Liu, A. Kahn, Y. Nao, *Nat. Energy* **2017**, *2*, 17104.

[5] A. Pérez-Rodríguez, *presented in NEXTGEN '19: 2019 Next Generation High Efficiency Photovoltaics International School and Workshop*, Mallorca, October 2019.

[6] K. Ellmer, A. Bikowski, *J. Phys. D.: Appl. Phys.* **2016**, *49*, 413002.

[7] M. Grundmann, F. Klüpfel, R. Karsthof, P. Schlupp, F. L. Schein, D. Splith, C. Yang, S. Bitter, H. Von Wenckstern, *J. Phys. D. Appl. Phys.* **2016**, *49*, 21.

[8] D. K. Ban, M. Patel, T. T. Nguyen, J. Kim, *Adv. Electron. Mater.* **2019**, *5*, 1900348.

[9] T. T. Nguyen, M. Patel, J. W. Kim, W. Lee, J. Kim, *J. Alloys Compd.* **2020**, *816*, 152602.

[10] R. Karsthof, P. Räcke, H. Von Wenckstern, M. Grundmann, *Phys. Status Solidi A* **2016**, *213*, 30.

[11] R. Karsthof, H. von Wenckstern, M. Grundmann, *J. Vac. Sci. Technol. B* **2016**, *34*, 04J107.

[12] M. Patel, H. S. Kim, J. Kim, J. H. Yun, S. J. Kim, E. H. Choi, H. H. Park, *Sol. Energy Mater. Sol. Cells* **2017**, *170*, 246.

[13] L. Han, X. Zhao, M. Ma, F. Gao, X. Xun, Q. Liao, Z. Zhang, Z. Kang, Y. Zhang, *Nano Energy* **2019**, *57*, 528.

[14] Ü. Özgür, Y. I. Alivov, C. Liu, A. Teke, M. A. Reshchikov, S. Doğan, V. Avrutin, S.-J. J. Cho, H. Morkoç, S. Doğan, V. Avrutin, S.-J. J. Cho, H. Morkọ, *J. Appl. Phys.* **2005**, *98*, 041301.

[15] E. Schiff, *Sol. Energy Mater. Sol. Cells* **2003**, *78*, 567.

[16] M. Liu, M. B. Johnston, H. J. Snaith, *Nature* **2013**, *501*, 395.

[17] S. A. Veldhuis, P. P. Boix, N. Yantara, M. Li, T. C. Sum, N. Mathews, S. G. Mhaisalkar, *Adv. Mater.* **2016**, *28*, 6804.

[18] A. M. Elseman, C. Xu, Y. Yao, M. Elisabeth, L. Niu, L. Malavasi, Q. Liang Song, *Sol. RRL* **2020**, *4*, 2000136.

[19] W. Shockley, H. J. Queisser, *J. Appl. Phys.* **1961**, *32*, 510.

[20] M. Burgelman, P. Nollet, S. Degrave, *Thin Solid Films* **2000**, *361–362*, 527.

[21] C. Persson, C. Platzer-Björkman, J. Malmström, T. Törndahl, M. Edoff, *Phys. Rev. Lett.* **2006**, *97*, 146403.

[22] M. Guc, M. Neuschitzer, D. Hariskos, A. Bauer, W. Witte, W. Hempel, L. Calvo-Barrio, P. Pistor, A. Perez-Rodriguez, V. Izquierdo-Roca, *RSC Adv.* **2016**, *6*, 24536.

[23] A. Polity, B. K. Meyer, T. Krämer, C. Wang, U. Haboeck, A. Hoffmann, *Phys. Status Solidi A* **2006**, *203*, 2867.

[24] G. Baldissera, C. Persson, *J. Appl. Phys.* **2016**, *119*, 045704.

[25] R. Cuscó, E. Alarcón-Lladó, J. Ibáñez, L. Artús, J. Jiménez, B. Wang, M. J. Callahan, *Phys. Rev. B* **2007**, *75*, 165202.

[26] A. Bechlaghem, B. Zebentout, Z. Benamara, *Results Phys.* **2018**, *10*, 650.

[27] A. Gusain, R. M. Faria, P. B. Miranda, *Front. Chem.* **2019**, *7*, 61.

[28] W. Tress, K. Leo, M. Riede, *Adv. Funct. Mater.* **2011**, *21*, 2140.

[29] W. Tress, O. Inganäs, *Sol. Energy Mater. Sol. Cells* **2013**, *117*, 599.

[30] A. Wagenpfahl, D. Rauh, M. Binder, C. Deibel, V. Dyakonov, *Phys. Rev. B* **2010**, *82*, 115306.

[31] W.-I. Jeong, Y. E. Lee, H.-S. Shim, T.-M. Kim, S.-Y. Kim, J.-J. Kim, *Adv. Funct. Mater.* **2012**, *22*, 3089.